ACS OMEGA

Article

Cite This: ACS Omega 2018, 3, 724−733

Carboxylate Functional Groups Mediate Interaction with Silver Nanoparticles in Biofilm Matrix

Olga Sambalova,[†,∥] Kerstin Thorwarth,[‡] Norbert Victor Heeb,[†] Davide Bleiner,[†] Yucheng Zhang,[§] Andreas Borgschulte,*[,†,∥] and Alexandra Kroll*[,⊥]

[†]Laboratory for Advanced Analytical Technologies, [‡]Coating Competence Center, and [§]Electron Microscopy Centre, Empa, Ueberlandstrasse 129, 8600 Dübendorf, Switzerland

[∥]Department of Chemistry, University Zürich, Winterthurerstrasse 190, 8057 Zürich, Switzerland

[⊥]Department of Environmental Toxicology, EAWAG, Ueberlandstrasse 133, 8600 Dübendorf, Switzerland

Supporting Information

ABSTRACT: Biofilms causing medical conditions or interfering with technical applications can prove undesirably resistant to silver nanoparticle (AgNP)-based antimicrobial treatment, whereas beneficial biofilms may be adversely affected by the released silver nanoparticles. Isolated biofilm matrices can induce reduction of silver ions and stabilization of the formed nanosilver, thus altering the exposure conditions. We thus study the reduction of silver nitrate solution in model experiments under chemically defined conditions as well as in stream biofilms. Formed silver nanoparticles are characterized by state-of-the art methods. We find that isolated biopolymer fractions of biofilm organic matrix are capable of reducing ionic Ag, whereas other isolated fractions are not, meaning that biopolymer fractions contain both reducing agent and nucleation seed sites. In all of the investigated systems, we find that silver nanoparticle−biopolymer interface is dominated by carboxylate functional groups. This suggests that the mechanism of nanoparticle formation is of general nature. Moreover, we find that glucose concentration within the biofilm organic matrix correlates strongly with the nanoparticle formation rate. We propose a simple mechanistic explanation based on earlier literature and the experimental findings. The observed generality of the extracellular polymeric substance/AgNP system could be used to improve the understanding of impact of Ag^+ on aqueous ecosystems, and consequently, to develop biofilm-specific medicines and bio-inspired water decontaminants.

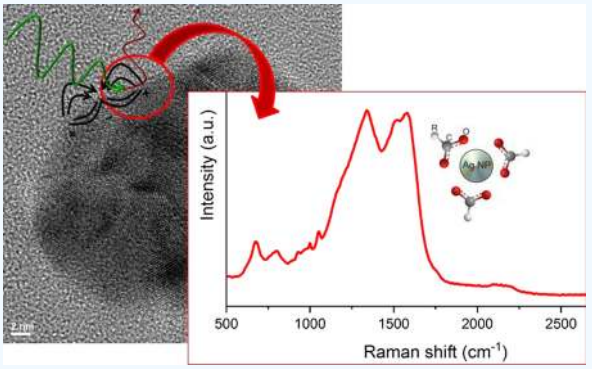

INTRODUCTION

Biofilms formed by microorganisms are ubiquitous at natural and anthropogenic surfaces. Biofilm-organized microorganisms can be detrimental to the anthropogenic infrastructure (biofouling) in different health conditions and medical applications due to superior mechanical properties, making biofilms more resistant to removal than loosely associated individuals.[1] Nonetheless, biofilms are at the basis of technical applications (e.g., in wastewater treatment, bioreactors/biofuel production[2]) and serve essential ecosystem functions, e.g., in streams.[3,4] Stream biofilms are primarily formed by bacteria and algae, with the specific composition being determined by environmental conditions.[5] They contribute to oxygen production and nutrient cycling, influence nearbed hydraulics, and serve as a habitat for different life forms.[6,7] Silver ions have long been known as potent bactericide with silver nanoparticles (AgNP) being increasingly used as a source of Ag^+ to avoid biofilm formation and for long-term antibacterial activity. Toxic effects of Ag to microorganisms have been reported extensively.[8] Ecologically and technically relevant microorganisms have been assessed for their sensitivity to Ag. For instance, in the algae *Chlamydomonas reinhardtii*, carbonate-stabilized AgNP decrease growth and photosynthetic activity more than Ag^+.[9] In stream biofilms, AgNP exerts antimicrobial effects stronger than or similar to Ag^+.[10] The integrity of biofilms is mediated by an extracellular organic matrix containing extracellular polymeric substances (EPS) like polysaccharides, glycoproteins, low-molecular-weight acids (LMWA), and neutral/amphiphilic compounds.[11,12] EPS act as the first line of contact to Ag. *Escherichia coli*, bacteria in activated sludge and marine diatoms showed an increase in EPS production when exposed to AgNP.[13−15] EPS may fundamentally alter the exposure to bactericidal Ag by reducing Ag^+ to AgNP and stabilizing the latter within its matrix, as shown with EPS from heterotrophic bacteria and stream biofilms.[16−18] The mechanism of interaction of AgNP with EPS and thus its potential

Received: July 12, 2017
Accepted: December 27, 2017
Published: January 22, 2018

DOI: 10.1021/acsomega.7b00982
ACS Omega 2018, 3, 724−733

Scheme 1. Simplified Reaction Mechanism of Ag^+ Reduction with Glc (A) Used as Reducing Agent[26,28−30] alongside the Reduction Potential of the Reaction[43,44] and Proposed Reaction Mechanisms with GlcA (B) and NAG (C) instead of Glc, Explaining the Observed Relative Reaction Rates: Glc > NAG > GlcA[a]

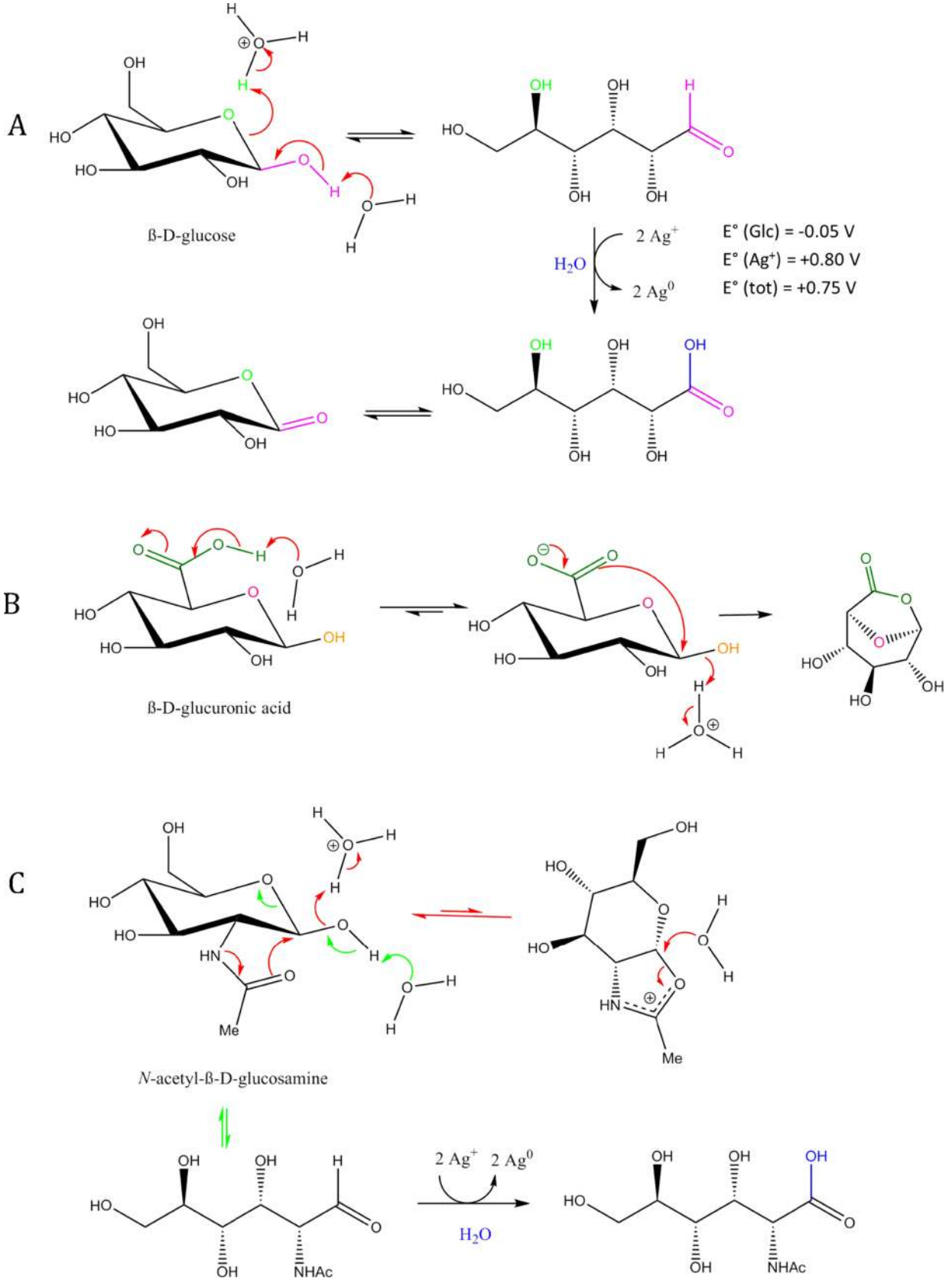

[a]The latter triggers no NP formation.

DOI: 10.1021/acsomega.7b00982
ACS Omega 2018, 3, 724−733

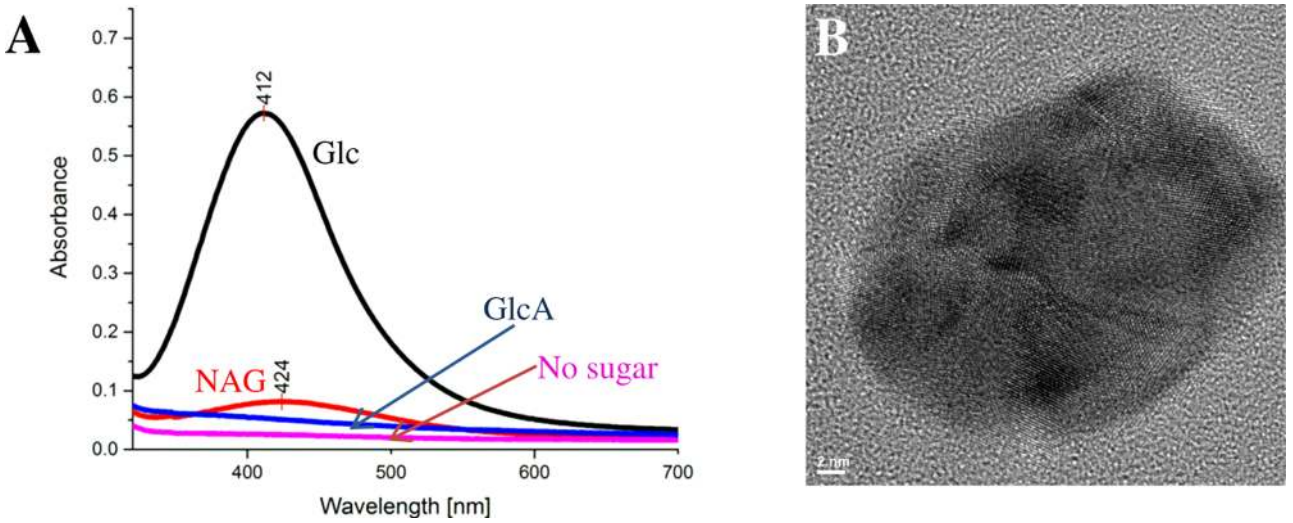

Figure 1. A: Representative UV−vis spectra of $AgNO_3$ in the presence of starch, with one of the following reducing sugars: Glc (black), NAG (red), GlcA (blue), and no sugar (pink). Samples were taken after 2 h of reaction. The peaks at 412 and 424 nm are characteristic of nanosilver surface plasmon resonance effect.[59] AgNP concentration contributes to the absorbance intensity, whereas NPs' core sizes refer to both the absorbance intensity and the nanoparticle size.[59] Thus, Glc resulted in a higher rate of nanoparticle formation than NAG, whereas GlcA and no reducing sugar lead to no nanoparticle formation. B: TEM image of AgNP embedded in the field EPS matrix. The nanosilver atoms are distinguishable; however, the organic matrix atoms are nonidentifiable. This image is representative for AgNPs imbedded in EPS matrix and starch.

specificity are unknown. We argue that knowledge on this interaction is needed to better understand the potential adverse environmental effects of Ag and develop targeted anti-biofilm compounds.

Operando analysis of such interface reactions in aqueous solutions is a great challenge. This is the result of the thick layers of molecules that usually surround the atomically thin interface. The probe beam must be capable of penetrating the surrounding layers, i.e., without strong interaction with the material of this layer, but still be sensitive enough to obtain information on the interface. Furthermore, most surface science techniques require high vacuum.[19] Optical spectroscopy can provide information about the systems in an aqueous environment.[20,21] However, the challenge of confining the signal to the atomic interface between covering layer and Ag surface remains. To overcome this challenge, resonance methods are applicable, such as surface-enhanced Raman spectroscopy (SERS). The Raman excitation from the molecules attached to the Ag surface is greatly enhanced as the result of a stronger electric field present directly at the NP surface, due to the resonant coupling of the conduction band electrons to the incident laser light (surface Plasmon resonance).[22,23] The enhancement is a local phenomenon and decays drastically within a few angstroms into the bulk and the medium.[22,24] SERS is thus a local probe of the molecules in the direct vicinity of the AgNP surface.

Our approach consisted of characterization of AgNP formation in the presence of a model polysaccharide and EPS extracted from natural biofilms with and without the commonly bioavailable reducing agents with UV−vis spectroscopy, dynamic light scattering (DLS), and NP tracking analysis (NTA). Characterization of functional groups interacting with AgNP was conducted using surface-enhanced Raman spectroscopy (SERS). Also, the oxidation state of formed nanosilver was probed with UV−vis spectroscopy, X-ray photoelectron spectroscopy (XPS), and transition electron microscopy (TEM).

RESULTS AND DISCUSSION

We develop a hypothesis of reaction mechanisms facilitating the AgNP formation and subsequent stabilization within the EPS matrix of stream biofilms (Scheme 1) based on the earlier knowledge of aldehyde-facilitated reduction of Ag^+ and other transition metal ions,[26−30] as well as multifactorial AgNP/EPS system bulk and interface analysis as described below. In general, chemically facilitated formation of nanosilver from Ag salts requires a reducing agent and a nucleation seed site.[31,32] Within the EPS matrix, the role of the latter could be played by the largest constituent—polysaccharides,[33,34] whereas terminating sugars and saccharide monomers could act as reducing agents.[35,36] Other biopolymers (BPs), such as collagen,[37,38] chitosan,[33] and poly(vinylpyrrolidone) (PVP),[39] have previously been used as stabilizing agents for AgNPs. A range of reducing agents have similarly been reported, e.g., sodium borohydride ($NaBH_4$),[40] *N*,*N*-dimethylformamaide,[41] and glucose.[35] Therefore, for the model system, we concentrated on the EPS matrix components that could represent the reducing agent and nucleation seed site system. The reaction under investigation consists of $AgNO_3$ in presence of one of the following monosaccharides, which act as reducing agents: *β*-D-glucose (Glc), *β*-D-glucuronic acid (GlcA), and *N*-acetyl-D-glucosamine (NAG), whereas starch is used as the model seed site and stabilizing agent.[25]

In the absence of starch, no NP formation is detected, signifying that polysaccharides are indispensable for NP formation. For spherical Ag nanoparticles, the plasmon absorption is centered at around 400 nm,[42] which is in agreement with the obtained UV−vis spectra (Figure 1A). In particular, the latter shows that Glc leads to fastest growth rate of AgNPs, resulting also in larger NPs than if other reducing sugars are used. These results are supported by NTA and DLS (Table S4, SI). The second fastest NP formation rate is observed with NAG, whereas GlcA deactivates the process of Ag^+ reduction and no AgNP formation is observed (Figure 1A).

To develop a hypothesis of the Ag^+ reduction mechanism, we consider our observations described further and the published

DOI: 10.1021/acsomega.7b00982
ACS Omega 2018, 3, 724−733

mechanism of aldehyde oxidation[26−30] (Scheme 1A). Glc is a known reducing sugar and capable of reducing Ag^+ to Ag^0 with the overall standard reduction potential of E^0 = +0.75 V (vs SHE).[43,44] The simplified reaction mechanism is presented in Scheme 1A.[26−28] Briefly, anomeric carbon of the Glc is oxidized to form carboxylic acid, whereas Ag^+ is reduced to Ag^0, which is the first step of a NP growth process.[45] The process then involves nucleation of the new crystals and crystal growth via agglomeration or monomer addition to form AgNP.[43] The final step involves passivation of the capping agents. It is likely that the Ag^+ reduction step proceeds via radical formation[46] and, indeed, light is indispensable for AgNP formation at the given reactant concentrations. However, for the sake of simplicity, we ignore the multitude of intermediate steps, as further experimental evidence would need to be provided to draw concrete conclusions.

GlcA (Scheme 1B), though structurally similar to Glc (Scheme 1A), has a carboxylic acid functional group instead of a hydroxyl group on C6. We hypothesize that the absence of AgNP formation may be due to the intramolecular reaction, which results in a loss of the anomeric center, and therefore the reducing ability, of GlcA (Scheme 1B).

NAG reduces Ag^+, however, with hindered reduction rates compared to the reduction with Glc. This could be explained by an intramolecular process (Scheme 1C) in which the doubly ringed compound is formed by the reaction of amide functional group on C2 with the C1 of the sugar. However, the formed complex bears a positive charge and therefore is prone to opening, after which a redox reaction may follow, alike the intermolecular reaction path with Glc (Scheme 1A).

The reducing sugars used in the model experiments are representative of the saccharides commonly found in the extracellular polymeric substance (EPS) of benthic biofilms.[47,48] To establish the relevance of the model to the environmental samples, *in situ* nanosilver formation facilitated by the EPS extracted from biofilms colonized in river Chriesbach, Switzerland, and collected from 12 different field sites (Figure 3B; Table S1, SI) is examined. Three replicas from each site are taken (noted later as A, B, and C). Liquid chromatography−organic carbon detection−organic nitrogen detection (LC−OCD−OND) analysis identifies the similarity of most biological replicas illustrating homogeneity along the stream (Figures S1 and S2, Table S3, SI). In the presence of 3.5 mM $AgNO_3$, 21 out of 36 EPS samples trigger the formation of AgNP within 12 days (Table S5, SI).

To identify the components essential to AgNP formation, the EPS samples are fractionated into biopolymers (BP), building blocks (BB) of humic acids, low-molecular-weight acids (LMWA), and neutral/amphiphilic (NA) compounds (Figure 2), and each fraction is reacted separately with $AgNO_3$.[12] It was found that the isolated biopolymer fraction is capable of reducing ionic Ag, whereas other isolated fractions are not, indicating that biopolymers within the EPS play a crucial role in the reduction process and must contain both the nucleation seed site, possibly relatively bulky polysaccharides, and the reducing agent, possibly the terminating sugars of the polysaccharide chains.

Based on the model study, we hypothesize that within the biopolymer fraction, Glc could be the driving reductant. Quantification of Glc in the EPS samples results in measured concentrations of 1.572−151.5 μM (Table S5, SI), which are 2−4 orders of magnitude lower than the concentration used in the model study (10.6 mM). However, a glucose assay indicates

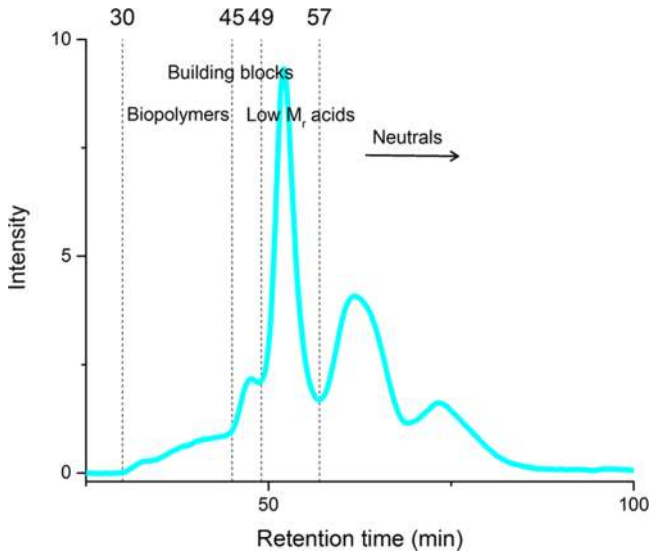

Figure 2. Characteristic LC−OCD−OND spectrum of EPS extracted from field biofilm samples. Peaks represent different fractions of EPS: biopolymers, building blocks of humic acids, low-molecular-weight acids, and neutral compounds.[12]

a clear correlation between the NP formation rate and concentration of the glucose in the EPS (Figure 3A; Table S5, SI). The other parameters, such as Cl^- concentration (Table S2, SI), do not seem to have a significant effect. Ten EPS samples that trigger AgNP formation within 4 or 8 days contain detectable amounts of Glc, whereas nine samples with AgNP formation after 12 days do not contain Glc above the detection limit (0.156 μM) (Figure 3A; Table S5, SI). The highest detected Glc concentrations coincide with a reaction within 4 days (91.3 and 151.5 μM Glc). Exceptions are samples A and C taken from site 3, which trigger NP formation after 8 days but do not contain detectable Glc. These stand out neither regarding EPS concentration of fractions and protein nor regarding measured species composition (Table S3, SI). We conclude that Glc probably is the main reducing agent in all of the AgNP-positive samples except those taken from site 3, which probably contain other low-molecular-weight reductants or reducing functional groups.

It is known that the specificity of the reducing and stabilizing agents will affect the nanoparticle size, polydispersity, and surface charge.[49,50] These parameters were taken into account via the analysis by NTA, DLS, and TEM. The results show that the formed NPs are in the size range of 60−200 nm (Table S4, SI) with the zeta-potential (ZP) values ranging from −22 to −30 mV (Table S4, SI), though TEM imaging allows for the identification of smaller NPs also (<10 nm; Figure S5C−E, SI). These results are in agreement with the previously reported systems.[46,51] However, although these factors are useful for describing variability between the systems, they carry no information on the redox reaction taking place at the AgNP−EPS interface. Therefore, there is a need for surface-sensitive techniques to further understand the systems on a molecular scale.

Surface-enhanced Raman spectroscopy (SERS) is a local probe of the molecules in the direct vicinity of a AgNP surface.[52] The SERS spectra of starch/Glc/AgNP complex (model system) and all of the field and colonized EPS/AgNP complexes show two prominent peaks at 1361 and 1572 cm^{-1} (Figure 4), which are not present in the absence of AgNP. The

DOI: 10.1021/acsomega.7b00982
ACS Omega 2018, 3, 724−733

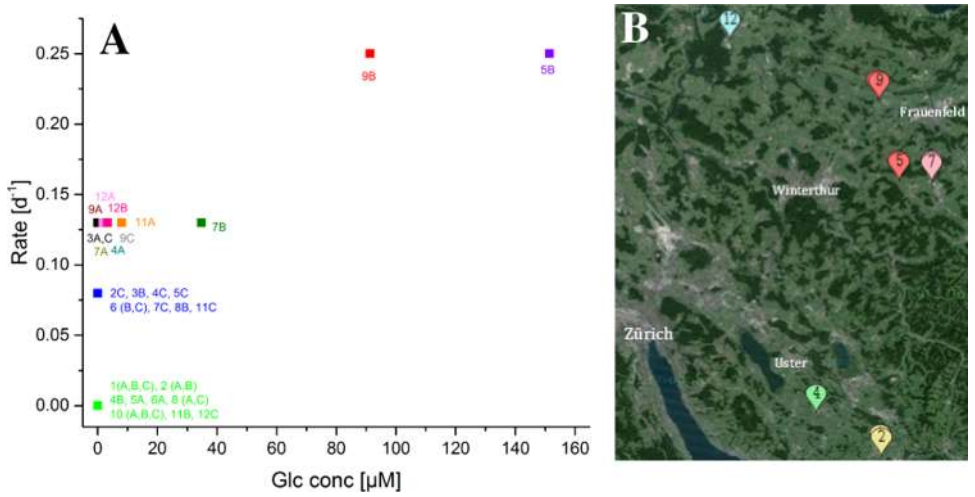

Figure 3. A: Graph representing dependence of AgNP formation reaction rate on the concentration of glucose within the EPS matrix. Number refers to collection site (B), whereas letters A−C denote three different samples collected at each site. With the exception of samples 3A and 3C, a higher glucose concentration resulted in a higher rate of NP formation. B: Map illustrating the 12 sampling sites (6 up- and 6 downstream from wastewater treatment plant; noted by numbers 1−12) used for the collection of stream biofilms. Three samples per site were collected (noted as A, B, and C).

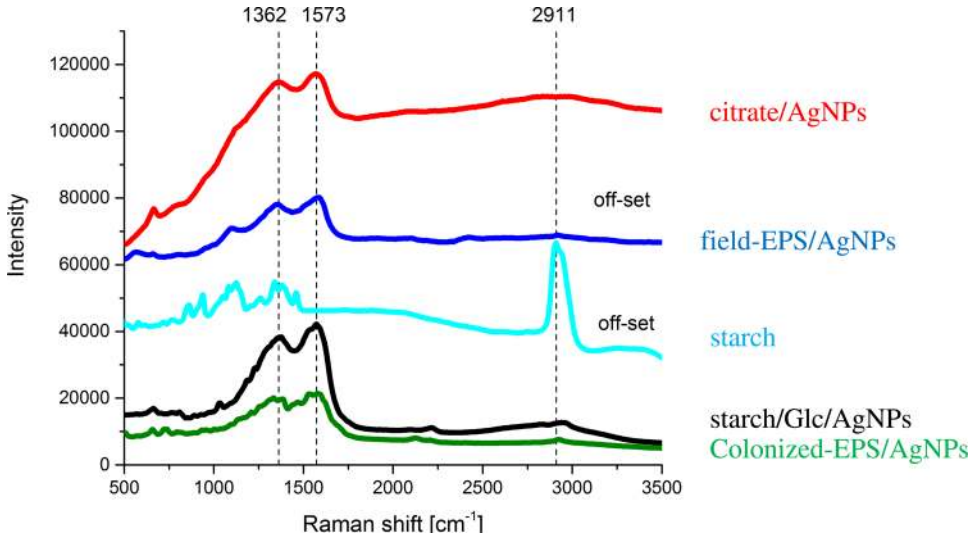

Figure 4. SERS spectra of starch (cyan) and AgNP stabilized by citrate (red), field EPS (blue), starch/Glc (black), and colonized EPS (green) systems. The starch peak at 2911 cm^{-1} (assigned as CH stretching vibrations) can be used as a reference: in the presence of AgNP (starch/Glc) system, the intensity of otherwise prominent CH peak is negligible compared to highly amplified signals at 1362 and 1573 cm^{-1} (assigned as COO$^-$ stretching vibrations).[36] The amplification of the signal is due to the SERS effect, signifying close proximity of the COO$^-$ functional groups to the AgNP surface. The prominent amplification of the COO$^-$ groups is also observed in AgNP stabilized by citrate (known to be stabilized by COO$^-$; used as reference), as well as colonized and field EPS. This suggests that EPS supports the formed NP primarily by COO$^-$ functional groups.

degree of enhancement is especially evident when considering the CH stretching peak of starch at 2911 cm^{-1}, which is prominent in starch in the absence of AgNP, but negligible compared to the peaks at 1361 and 1572 cm^{-1} (Figure 4). The latter are assigned as the symmetric and asymmetric stretching of the carboxylate functional groups, respectively.[36] The assignment is further confirmed against the commercially available citrate and carbonate AgNP, which are known to stabilize AgNP via carboxylate functional groups. The SERS spectra of these complexes show the same two strong peaks at 1361 and 1572 cm^{-1} (Figure S4, SI). The exclusive enhancement of the COO$^-$ vibrations by the surface plasmons is in agreement with a binding of one or even two oxygen atoms of a carboxylate group to Ag.[53] Thus, metallic AgNP is surrounded primarily by the carboxylate functional groups of the EPS matrix. This was found to be true regardless of the EPS fractional composition, which is analyzed by LC−OCD−OND (Table S3, SI). It is well known that AgNPs can be stabilized by the carboxylic acid groups of yeast[54] and other biomolecules.[50] However, the general selectivity of stabilizing groups observed for all of the EPS may be surprising. The general presence of carboxylate groups at the AgNP surface could be explained by considering the redox process of NP formation, where the reducing sugar is oxidized to form carboxylate functional groups, which then stabilize the NP.

The EPS/AgNP as well as model samples has the characteristic yellow color from plasmon absorbance, which is indicative of nonoxidized silver surface.[46,51] However, it is well known that AgNPs in aqueous environment are unstable due to agglomeration and surface oxidation of the particles.[36,55,56] To

DOI: 10.1021/acsomega.7b00982
ACS Omega 2018, 3, 724−733

further characterize the Ag surface and especially probe the oxidation state of the silver, we utilize the X-ray photoelectron spectroscopy (XPS) (Figure 5) and electron diffraction (Figure S5B, SI). The XPS spectrum allows identification of Ag, C, O, N, Na, and Ca atoms present in the EPS/AgNP samples (Figure 5). The Ag $3d_{5/2}$ peak at 368 eV is characteristic of nonoxidized Ag.[57] However, due to the broadness of the peak, no definite conclusion can be drawn and the peak may consist of multiple overlapping peaks.[57] In addition, electron diffraction identifies Ag(111) and Ag(002) facets, which are characteristic of nonoxidized Ag (Figure S5B, SI). Yet, both methods cannot exclude the existence of an oxidized silver surface, which is likely under these conditions. However, this does not undermine the SERS effect. It has been observed that intentionally oxidized Ag enhances the SERS effect compared to metallic Ag, which is explained by a stronger binding of the exciting molecules to an activated, i.e., oxidized, surface.[58]

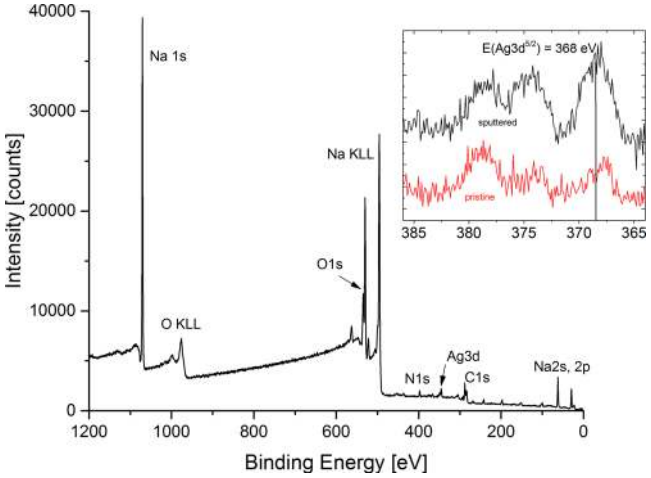

Figure 5. Representative X-ray photoelectron spectroscopy spectrum of AgNP embedded in the EPS matrix extracted from field biofilm samples after sputtering. The inset shows the enlargement of the Ag 3d region. The pristine sample is depicted in red, whereas the sputtered is shown in black. The peak at 368 eV is characteristic of metallic Ag, though the spectrum does not exclude the possibility of oxide layer on the surface, as the peak at 386 eV may consist of multiple overlapping signals.[57] Apart from Ag, the elements that are clearly identified by XPS are Na, C, O, and N.

The EPS/AgNP system is also studied by Fourier transform infrared (FTIR) (Figure S6, SI). Among others, the carboxylate peaks are clearly visible on the obtained spectra; however, the EPS without AgNPs also displays carboxylate peaks (1395 and 1653 cm^{-1}), and no conclusive information on the interface can be drawn from the method.

CONCLUSIONS

We studied the redox reaction of Ag nanoparticle formation and stabilization within EPS matrices extracted from benthic biofilms. We present the evidence that both reducing agent and nucleation seed site, possibly polysaccharides,[31] are found within the biopolymer fraction of EPS. Moreover, there is a clear correlation between the glucose concentration within the EPS and the Ag nanoparticle formation rate, as determined by UV−vis, NTA, and DLS. This suggests that glucose is a crucial reducing agent within the EPS. Another commonly bioavailable sugar, *N*-acetyl glucosamine (NAG), could also play a role in the redox process, whereas glucuronic acid showed no evidence of nanoparticle formation, as demonstrated by a model study with starch as the stabilizing polysaccharide. From an environmental perspective, we conclude that the resulting exposure of microorganisms to AgNP depends on the chemical and structural composition of the EPS. The interface of the formed NPs was characterized by SERS, and the presence of carboxylate functional groups at the NP surface was found to be perpetual for all of the EPS/AgNP systems. The generality of the interaction and the applicability of SERS method for interface analysis of AgNP in a complex biological environment is thus demonstrated. Based on these findings as well as earlier literature,[26−30] we present a hypothesis for plausible redox mechanism of EPS-facilitated reduction of ionic silver. The mechanism is based on the oxidation of aldehyde groups at the anomeric carbon of reducing sugar monomers to carboxylic acid groups. The latter then stabilize the surface of the formed Ag^0, which could explain the apparently omnipresent carboxylate functionalization of Ag surface in the EPS/AgNP mixture.

The observed generality of the EPS/AgNP system could be used to improve the understanding of specific responses of microorganisms to Ag based on their EPS composition, and consequently, to develop biofilm-specific medicines and bio-inspired water decontaminants. Thus, this study suggests that Ag ions can be used to eliminate harmful bacteria, if the EPS-mediated NP formation and stabilization via carboxylic acid groups is disrupted. This method would be making use of bactericidal properties of Ag ions, which are, however, harmless to mammalian cells. The same effect could also be industrially applicable for, e.g., removing biofilm formation on ship hulls or inside the water pipes. On the other hand, Ag ions can be efficiently trapped in the artificial or biological polymer matrix with a high number of carboxylic acid terminated surface functional groups. This could be useful in, e.g., wastewater treatment for achieving minimum environmental disturbance of the aquatic ecosystems.

MATERIALS AND METHODS

Chemicals. All of the chemicals were purchased from Sigma-Aldrich if not stated specifically below. Nanopure water (18.1 MΩ·cm, Milli-Q) was used as a solvent.

Silver nanoparticles with a nominal primary particle size of 25 nm were produced by wet precipitation from $AgNO_3$ in the presence of carbonate or citric acid by NanoSys GmbH (Wolfhalden, Switzerland) as an aqueous suspension with a nominal concentration of 1 g/L (9.27 mM) Ag. The original suspension was kept in the dark.

All of the nanoparticles were formed under irradiated conditions (light spectrum mimicking the sunlight spectrum). In the absence of light, no nanoparticle formation was observed on the chosen timeframe at the given concentrations. Blank experiments without the EPS yield no nanosilver, as well as not all of the EPS samples will trigger a nanoparticle formation, suggesting that the chemical composition of the EPS is of crucial importance for nanoparticle formation and stabilization.

Synthesis of EPS Stabilized Ag Nanoparticles. All of the silver nanoparticles were formed in situ in the UV−vis exposure system by the EPS extracted from periphyton. The UV−vis exposure system was constructed with a thermostat (Lauda RC6 RC), control stirrer module (H & P Labortechnik Variomag Telemodul 40-S), and a set of lamps (Philips Master TL5 HO 54W/865 SLV/40). The conditions used for nanoparticle synthesis were as follows: temperature 20 °C,

DOI: 10.1021/acsomega.7b00982
ACS Omega 2018, 3, 724−733

stirring 200 rpm, and light irradiation matching sunlight spectrum.

Silver Film Preparation. The samples were prepared using unbalanced direct current magnetron sputter deposition from an elemental Ag target with a purity of 5N in a UHV system at room temperature. The deposition chamber used is an ATC 1500 F sputtering system from AJA international Inc. (North Scituate, MA). The base pressure before deposition was $<5 \times 10^{-7}$ Pa; during deposition, the pressure was kept at 5.4 Pa using a constant Ar flow of 16 sccm. Silver was sputtered at a power density of 5.0 W/cm^2. Before deposition, the samples were cleaned using a radio frequency bias on the substrate of −250 V in flowing Ar (15 sccm) at a pressure of 0.5 Pa. The samples were grown to a thickness of 200 nm, as determined using a Bruker Dektak XT surface profilometer equipped with a diamond stylus.

Colonization of Stream Biofilms on Artificial Substrates and Sampling of Biofilms. Biofilms were colonized on glass microscope slides (38 × 26 mm^2, Thermo Scientific) which were placed vertically in river Chriesbach for 21 days (Dübendorf, Switzerland, 47°24′16.8″N, 8°36′41.0″E). For the extraction of extracellular polymeric substances, the biofilms were scraped off the glass slides with a clean glass slide into 1 mL/slide $NaHCO_3$ (2 mM, pH 7.6) in a glass beaker. The extracellular polymeric substances were extracted on the same day (see below).

Field Sampling of Stream Biofilms. The samples were taken on November 5 and 6, 2015, from six rivers in the Swiss Plateau upstream and downstream communal wastewater treatment plants (sites 1−12, Table S1 of SI, Figure 3B). Three stones of similar size from similar microenvironments in the river bed were selected at each sampling site. The biofilms were brushed off the stones with tooth brushes into 15 mL of stream water, which was sampled at the site and filtered through two layers of paper towel. The stones were washed with another 15 mL of filtered stream water. The extraction of extracellular polymeric substances was performed on the same day (see below).

Water Analytics. At each field sampling site, spot measures of physical parameters were taken roughly at the same distance above ground as the surfaces of the stones sampled. The water temperature was measured with a DIEHL frigoton thermometer and flow velocity with a Schiltknecht MiniAir2 Micro anemometer (flow accuracy 1.0% fs, 3.0% rdg).

Water chemistry of the grab samples (500 mL) taken from each sampling site and of the extracted EPS (see below) was determined as follows: Na^+, K^+, Ca^{2+}, Mg^{2+}, NO_3^{2-}, SO_4^{2-}, and Cl^- content was quantified by ion chromatography (Metrohm 761 Compact IC, with chemical suppression for NO_3^{2-}, SO_4^{2-}, and Cl^-), with a 8 mM HNO_3/1.197 mM dipicolinic acid solution as the mobile phase and a Metrosep C 6 − 250/4.0 separation column (Metrohm, Na^+, K^+, Ca^{2+}, and Mg^{2+}) or a Metrosep A Supp 5 100/4 mm column (Metrohm, NO_3^{2-}, SO_4^{2-}, and Cl^-) as the stationary phase. PO_4^{3-} was quantified colorimetrically (Varian Cary 50 Bio Spectrophotometer) based on the formation of molybdenum blue. Silica was determined colorimetrically based on the reduction of siliciomolybdate to silicomolybdous acid in the presence of ascorbic acid using the Autoanalyzer AA3, Bran + Luebbe (Contrec). TOC and DOC were measured with a shimadzu TOC-L CSH system. LOQ were 2.5 mg/L Na^+, 1 mg/L K^+, 5 mg/L Ca^{2+}, 2.5 mg/L Mg^{2+}, 0.5 mg/L NO_3^{2-}, 5 mg/L SO_4^{2-}, 0.5 mg/L Cl^-, 1 mg/L H_4SiO_4, and 0.5 mg/L OC.

Metal concentrations were determined by inductively coupled plasma mass spectrometry (ICP-MS) after microwave digestion. 0.5 mL of each sample was digested with 4 mL of 65% HNO_3 and 0.5 mL of 30% H_2O_2 in a microwave digestion unit (MLS ultraClave 4; 10 min at 180 °C/100 bar, 14 min at 210 °C/100 bar) and diluted 1:100 with nanopure water (18.1 MΩ·cm, Milli-Q). One sample per run contained only HNO_3 and H_2O_2 to determine the background concentration of target metals.

The target metal concentrations were measured by HR-ICP-MS (Element 2 High Resolution Sector Field ICP-MS; Thermo Finnigan). The instrument was calibrated with a multielement mass standard (Merck, 1113550100). The calibration curve for data analysis was made with the calibration standard Merck IV in the concentration range 0−20 μg/L. A reference with a concentration within the calibration range was measured every 10 samples, the calibration samples were measured every 40 samples.

Extraction, Characterization, and Fractionation of Extracellular Polymeric Substances (EPS) from Periphyton. The extraction procedure was performed as described previously.[5,9,25] The biomass was resuspended by gentle pipetting and sonication in a water bath (45 kHz, 60 W, VWR Ultrasonic Cleaner) for 30 s. Fine sediment and larger biomass was allowed to settle for ∼1 min, the supernatant was removed and centrifuged at 1880*g* for 10 min. Biomass was resuspended a second time in 2 mL/slide fresh solution and treated as described above. All of the supernatants were sequentially filtered (1 μm glass fiber [VWR], 0.45 μm polypropylene [PALL], and 0.22 μm PES [Millipore] filters). The filters were washed with nanopure water (18.1 MΩ·cm, Milli-Q) before use. EPS extracts were stored in glass bottles at 4 °C (0.02% (w/v) NaN_3). All of the extraction steps were performed on ice, and the water bath for ultrasound treatment was at room temperature.

Organic carbon and nitrogen size distribution was measured by size-exclusion chromatography−organic carbon detection−organic nitrogen detection (LC−OCD−OND) as described previously.[5,9] The samples were diluted with nanopure water (18.1 MΩ·cm, Milli-Q) right before they were measured. A size exclusion column (250 × 20 mm^2, Toyopearl TSK HW-50S) was used to separate the EPS compounds. The mobile phase was phosphate buffer (24 mM, pH 6.6), and the acidification solution was phosphoric acid (60 mM, pH 1.2). The detection limit was 10 μg/L for both OC and ON. The software FIFFIKUS was used to quantify the total organic carbon (TOC), dissolved (DOC), and chromatographable DOC compounds (cDOC). The chromatograms obtained from LC−OCD−OND were integrated to determine the amount of biopolymers (BP, high M_r polysaccharides, and proteins), building blocks of humic substances (BB), low M_r acids (LMWA), and amphiphilic/neutral compounds (NA, alcohols, aldehydes, amino acids, and ketones).

To separate the fractions BP, BB, LMWA, and NA, a Bio-Rad 2110 fractionator coupled to the LC−OCD−OND system was employed. Fractions were taken between retention times of 30−45 min (BP), 45−49 min (BB), 49−57 min (LMWA), and 57−80 min (NA).

Nanoparticle Tracking Analysis (NTA). Nanoparticle tracking analysis (NTA, NanoSight LM10 equipped with a LM14 temperature controller (NanoSight Ltd.)) was used to determine a number-based particle size distribution. Each sample was directly measured three times for 60 s. All of the

DOI: 10.1021/acsomega.7b00982
ACS Omega 2018, 3, 724−733

NTA videos were analyzed with the same settings in batch processing mode. Analyses that resulted in less than 200 tracked particles were not used. Videos were analyzed using the NanoSight NTA 2.3 Analytical Software (NanoSight Ltd.). Settings were as follows: background extract: on; brightness: 0; gain: 1; blur size: 9 × 9; detection threshold type: single; detection threshold: 15; min track lenth: 10; min expected size: auto; temperature: 23 °C; and viscosity: 0.9326.

Dynamic Light Scattering (DLS) and Zeta-Potential (ZP). Dynamic light scattering (DLS) and zeta-potential (ZP) were measured with a Malvern Instruments Nano ZS in polystyrene cuvettes. Each sample was measured at the temperature of 25 °C three times and the autocorrelation function was analyzed using the cumulant analysis algorithm resulting in a mean size (z-average) and a standard deviation (polydispersity index). The DLS measurements performed on aqueous suspension containing EPS did not indicate any particles.

UV−vis Absorption Spectra. UV−vis light absorption (190−900 nm) was recorded with a CARY 100 UV−vis spectrophotometer (Agilent Technologies) in microquartz cuvettes. AgNP show size- and surface-specific surface plasmon resonance, which results in a specific UV−vis absorption spectrum. The spectra were recorded in a solution with an optical path length of 10 mm.

Surface-Enhanced Raman Spectroscopy (SERS). Raman spectra were recorded with a Bruker SENTERRA Raman microscope with 532 nm 20 mW laser and 10× objective lens. Each sample was measured on glass slides for 180 s.

Fourier Transform Infrared Spectroscopy (FTIR). Infrared spectra were measured in solid state with a Cary 600 Series ATR-FTIR Spectrometer (Agilent Technologies). The average of 32 measurements was taken.

Transmission Electron Microscopy (TEM). Transmission electron microscopy (TEM) samples were prepared by casting one drop of the solution directly onto copper grids (TedPella, product number: 11824) with the carbon lacey network covered with a ∼3 nm thin carbon film. High-resolution TEM (HR-TEM) and selected area electron diffraction (SAED) were performed on a JEOL 2200FS microscope operated at 200 kV. Typically, 0.5 s exposure time was used for recording the HR-TEM images. No morphological change in the particles caused by the electron beam was observed during imaging and diffraction. An analysis of the images and diffraction patterns was performed using a DigitalMicrograph.

X-ray Photoelectron Spectroscopy (XPS). The samples were characterized by X-ray photoelectron spectroscopy (XPS) using a Quantum 2000 (Physical Electronics Inc.) instrument under ultrahigh vacuum ($<5 \times 10^{-7}$ Pa). Monochromatic Al Kα X-rays with a photon energy $h\nu$ = 1486.7 eV were used, and the data were recorded at an analyzer pass energy of 23.50 eV and a step size of 0.1 eV (for the detailed spectra) and a pass energy of 58.70 eV and a step size of 0.5 eV for the survey. Argon ions and electron neutralizers were used to compensate for surface charging.

The data were collected with (∼2 nm removed) and without sputter-cleaning to eliminate contaminations. The XPS background spectrum was checked with a CasaXPS software and found to be linear for the region of interest (365−375 eV).

Glucose Assay. Glucose concentration of extracted EPS samples was determined with a High Sensitivity Glucose Assay Kit (Sigma-Aldrich, MAK181) according to the procedure described by the manufacturer. In the presence of glucose, a fluorometric product is formed proportional to the glucose concentration. Of each sample, 1 and 10 μL were reacted in duplicate with the reaction mix in a final volume of 100 μL in 96-well plates. Fluorescence was measured with a Tecan plate reader (excitation: 535 nm, emission: 587 nm). Standard deviation of blanks was 0.0518 pmol/μL, detection limit was thus in the range of 0.156 pmol/μL. Spiking extracted EPS with glucose showed no interference with the assay above the detection limit.

■ ASSOCIATED CONTENT

Supporting Information

The Supporting Information is available free of charge on the ACS Publications website at DOI: 10.1021/acsomega.7b00982.

LC−OCD−OND chromatograms of starch, glucose, glucuronic acid, *N*-acetyl glucosamine, and each EPS sample from 12 sampling sites; relative composition of field EPS extracts as determined by LC−OCD−OND based on Table 3; characterization of nanoparticle dispersions obtained by reacting $AgNO_3$ with field EPS extracts; SERS spectra of nanoparticle controls (PVP, citrate, carbonate) and silver films; characterization of EPS-stabilized AgNPs (Figures S1−S6); FTIR spectra of pristine EPS (blue) and EPS-stabilized AgNPs (red) and FTIR peak assignment; sampling sites along Mönchaltorfer Aa; physicochemical characteristics of the sampling sites along Mönchaltorfer Aa; characterization of the EPS extracts by LC−OCD−OND, protein, and glucose quantification; characterization of nanoparticle dispersions obtained by reacting $AgNO_3$ with field EPS extracts; glucose concentration of extracted EPS samples compared to time elapsed until detectable NP formation; concentration of selected ions in extracted EPS samples [mg/L] (Tables S1−S6) (PDF)

■ AUTHOR INFORMATION

Corresponding Authors

*E-mail: andreas.borgschulte@empa.ch (A.B.).
*E-mail: alexandra.kroll@eawag.ch (A.K.).

ORCID

Yucheng Zhang: 0000-0003-3733-5851
Andreas Borgschulte: 0000-0001-6250-4667
Alexandra Kroll: 0000-0001-7214-5725

Author Contributions

The manuscript was written through contributions of all of the authors. All of the authors have given approval to the final version of the manuscript.

Funding

The presented work was supported by the Swiss National Science Foundation (SNSF) Ambizione grant PZ00P2_142533 to Alexandra Kroll.

Notes

The authors declare no competing financial interest.

■ REFERENCES

(1) Yan, J.; Sharo, A. G.; Stone, H. A.; Wingreen, N. S.; Bassler, B. L. *Vibrio cholerae* biofilm growth program and architecture revealed by single-cell live imaging. *Proc. Natl. Acad. Sci. U.S.A.* **2016**, *113*, E5337.

DOI: 10.1021/acsomega.7b00982
ACS Omega 2018, 3, 724−733

(2) Brenner, K.; You, L.; Arnold, F. H. Engineering microbial consortia: a new frontier in synthetic biology. *Trends Biotechnol.* **2008**, *26*, 483−489.
(3) Allan, J. D.; Castillo, M. M. *Stream Ecology*; Springer: Netherlands, 2007.
(4) Battin, T. J.; et al. Biophysical controls on organic carbon fluxes in fluvial networks. *Nat. Geosci.* **2009**, *2*, 595−595.
(5) Azim, M. E.; Asaeda, T. Periphyton Structure Diversity and Colonization. In *Periphyton: Ecology, Exploitation and Management*, 1st ed.; Azim, M. E., Verdegem, M. C. J., van Dam, A. A., Beveridge, M. C. M., Eds.; CABI, 2005; pp 15−34.
(6) Stevenson, R. J. An Introduction to Algal Ecology in Freshwater Benthic Habitats. In *Algal Ecology*; Academic Press, 1996; pp 3−30.
(7) Nikora, V. I.; Goring, D. G.; Biggs, B. J. F. Some observations of the effects of micro-organisms growing on the bed of an open channel on the turbulence properties. *J. Fluid Mech.* **2002**, *450*, 317−341.
(8) Petering, H. G. Pharmacology and toxicology of heavy metals: silver. *Pharmacol. Ther., Part A* **1976**, *1*, 127−130.
(9) Wagner, B.; et al. Toxicity of silver nanoparticles to *Chlamydomonas reinhardtii*. *Environ. Sci. Technol.* **2008**, *42*, 8959−64.
(10) Gil-Allué, C.; Schirmer, K.; Tlili, A.; Gessner, M. O.; Behra, R. Silver nanoparticle effects on stream periphyton during short-term exposures. *Environ. Sci. Technol.* **2015**, *49*, 1165−1172.
(11) Bellinger, B. J.; Gretz, M. R.; Domozych, D. S.; Kiemle, S. N.; Hagerthey, S. E. Composition of extracellular polymeric substances from periphyton assemblages in the Florida everglades. *J. Phycol.* **2010**, *46*, 484−496.
(12) Stewart, T. J.; Traber, J.; Kroll, A.; Behra, R.; Sigg, L. Characterization of extracellular polymeric substances (EPS) from periphyton using liquid chromatography-organic carbon detection-organic nitrogen detection (LC-OCD-OND). *Environ. Sci. Pollut. Res.* **2013**, *20*, 3214−3223.
(13) Joshi, N.; Ngwenya, B. T.; French, C. E. Enhanced resistance to nanoparticle toxicity is conferred by overproduction of extracellular polymeric substances. *J. Hazard. Mater.* **2012**, *241*−*242*, 363−370.
(14) Zhang, C.; Liang, Z.; Hu, Z. Bacterial response to a continuous long-term exposure of silver nanoparticles at sub-ppm silver concentrations in a membrane bioreactor activated sludge system. *Water Res.* **2014**, *50*, 350−358.
(15) Miao, A. J.; et al. The algal toxicity of silver engineered nanoparticles and detoxification by exopolymeric substances. *Environ. Pollut.* **2009**, *157*, 3034−3041.
(16) Kroll, A.; Behra, R.; Kaegi, R.; Sigg, L. Extracellular polymeric substances (EPS) of freshwater biofilms stabilize and modify CeO2 and Ag nanoparticles. *PLoS One* **2014**, *9*, No. e110709.
(17) Kang, F.; Alvarez, P. J.; Zhu, D. Microbial Extracellular Polymeric Substances Reduce Ag^{+} to Silver Nanoparticles and Antagonize Bactericidal Activity. *Environ. Sci. Technol.* **2014**, *48*, 316−322.
(18) Ivask, A.; et al. Size-dependent toxicity of silver nanoparticles to bacteria, yeast, algae, crustaceans and mammalian cells in vitro. *PLoS One* **2014**, *9*, No. e102108.
(19) Somorjai, G. A.; Li, Y. Electrical properties of surfaces. In *Introduction to Surface Chemistry and Catalysis*, 2nd ed.; John Wiley & Sons: New York, 2010; pp 362−399.
(20) Desilvestro, J.; Weaver, M. J. Surface structural changes during oxidation of gold electrodes in aqueous media as detected using surface-enhanced Raman spectroscopy. *J. Electroanal. Chem. Interfacial Electrochem.* **1986**, *209*, 377−386.
(21) Pottier, A.; et al. Size tailoring of TiO2 anatase nanoparticles in aqueous medium and synthesis of nanocomposites. Characterization by Raman spectroscopy. *J. Mater. Chem.* **2003**, *13*, 877−882.
(22) Dieringer, J. A.; et al. Introductory Lecture: Surface enhanced Raman spectroscopy: new materials, concepts, characterization tools, and applications. *Faraday Discuss.* **2006**, *132*, 9−26.
(23) Yee, S. S. Surface plasmon resonance sensors: review. *Sens. Actuators, B* **1999**, *54*, 3−15.
(24) Hutter, E.; Fendler, J. H. Exploitation of localized surface plasmon resonance. *Adv. Mater.* **2004**, *16*, 1685−1706.
(25) Raveendran, P.; Fu, J.; Wallen, S. L. Completely 'Green' Synthesis and Stabilization of Metal Nanoparticles Completely 'Green' Synthesis and Stabilization of Metal Nanoparticles. *J. Am. Chem. Soc.* **2003**, *125*, 13940−13941.
(26) Benet, W. E.; Lewis, G. S.; Yang, L. Z.; Hughes, P. D. E. The mechanism of the reaction of the Tollens reagent. *J. Chem. Res.* **2011**, *35*, 675−677.
(27) Sarkar, A.; Kapoor, S.; Mukherjee, T. Synthesis and characterisation of silver nanoparticles in viscous solvents and its transfer into non-polar solvents. *Res. Chem. Intermed.* **2010**, *36*, 411−421.
(28) Gomes, J. F.; et al. New insights into the formation mechanism of Ag, Au and AgAu nanoparticles in aqueous alkaline media: alkoxides from alcohols, aldehydes and ketones as universal reducing agents. *Phys. Chem. Chem. Phys.* **2015**, *17*, 21683−21693.
(29) Chou, K.-S.; Ren, C.-Y. Synthesis of nanosized silver particles by chemical reduction method. *Mater. Chem. Phys.* **2000**, *64*, 241−246.
(30) Fievet, F.; et al. Homogeneous and heterogeneous nucleations in the polyol process for the preparation of micron and submicron size metal particles. *Solid State Ionics* **1989**, *33*, 198−205.
(31) Patakfalvi, R.; Papp, S.; Dékány, I. The kinetics of homogeneous nucleation of silver nanoparticles stabilized by polymers. *J. Nanopart. Res.* **2007**, *9*, 353−364.
(32) Thanh, N. T. K.; Maclean, N.; Mahiddine, S. Mechanisms of nucleation and growth of nanoparticles in solution. *Chem. Rev.* **2014**, *114*, 7610−7630.
(33) Ikuma, K.; Madden, A. S.; Decho, A. W.; Lau, B. L. T. Deposition of nanoparticles onto polysaccharide-coated surfaces: implications for nanoparticle−biofilm interactions. *Environ. Sci. Nano* **2014**, *1*, 117.
(34) Flemming, H.-C.; Wingender, J. The biofilm matrix. *Nat. Rev. Microbiol.* **2010**, *8*, 623−633.
(35) Shi, Y. L.; Zhou, Q.; Lv, L. Y.; Hong, W. A Facile Method for the Synthesis of Silver Nanoparticles in the Presence of Sodium Phosphate. *Appl. Mech. Mater.* **2011**, *109*, 174−177.
(36) Ortega-Arroyo, L.; et al. Green synthesis method of silver nanoparticles using starch as capping agent applied the methodology of surface response. *Starch/Staerke* **2013**, *65*, 814−821.
(37) Alarcon, E. I.; et al. Coloured cornea replacements with anti-infective properties: expanding the safe use of silver nanoparticles in regenerative medicine. *Nanoscale* **2016**, *8*, 6484−6489.
(38) Alarcon, E. I.; et al. Safety and efficacy of composite collagen−silver nanoparticle hydrogels as tissue engineering scaffolds. *Nanoscale* **2015**, *7*, 18789−18798.
(39) Wang, H.; Qiao, X.; Chen, J.; Ding, S. Preparation of silver nanoparticles by chemical reduction method. *Colloids Surf., A* **2005**, *256*, 111−115.
(40) Song, K. C.; Lee, S. M.; Park, T. S.; Lee, B. S. Preparation of colloidal silver nanoparticles by chemical reduction method. *Korean J. Chem. Eng* **2009**, *26*, 153−155.
(41) Jia, H.; Zeng, J.; An, J.; Xu, W.; Zhao, B. Surface-enhanced Raman activity and stability study of silver films prepared by reduction of Ag+ ions in N,N-dimethylformamide. *J. Colloid Interface Sci.* **2005**, *292*, 455−461.
(42) Stamplecoskie, K. G.; Scaiano, J. C.; Tiwari, V. S.; Anis, H. Optimal Size of Silver Nanoparticles for Surface-Enhanced Raman Spectroscopy. *J. Phys. Chem. C* **2011**, *115*, 1403−1409.
(43) Pacioni, N. L.; Borsarelli, C. D.; Rey, V.; Veglia, A. V. Synthetic Routes for the Preparation of Silver Nanoparticles. In *Silver Nanoparticle Applications*; Alarcon, E. I., Griffith, M., Udekwu, K. I., Ed.; Springer, 2015; pp 13−46.
(44) Shapley, P. Reduction Potentials, 2012. http://butane.chem.uiuc.edu/pshapley/genchem2/b9/2.html.
(45) Darroudi, M.; Ahmad, M. B.; Abdullah, A. H.; Ibrahim, N. A.; Shameli, K. Effect of accelerator in green synthesis of silver nanoparticles. *Int. J. Mol. Sci.* **2010**, *11*, 3898−3905.
(46) Alarcon, E. I.; et al. The biocompatibility and antibacterial properties of collagen-stabilized, photochemically prepared silver nanoparticles. *Biomaterials* **2012**, *33*, 4947−4956.

DOI: 10.1021/acsomega.7b00982
ACS Omega 2018, 3, 724−733

(47) Rossi, F.; De Philippis, R. Role of Cyanobacterial Exopolysaccharides in Phototrophic Biofilms and in Complex Microbial Mats. *Life* **2015**, *5*, 1218−1238.
(48) Staats, N.; De Winder, B.; Stal, L.; Mur, L. Isolation and characterization of extracellular polysaccharides from the epipelic diatoms *Cylindrotheca closterium* and *Navicula salinarum*. *Eur. J. Phycol.* **1999**, *34*, 161−169.
(49) Poblete, H.; et al. New Insights into Peptide-Silver Nanoparticle Interaction: Deciphering the Role of Cysteine and Lysine in the Peptide Sequence. *Langmuir* **2016**, *32*, 265−273.
(50) Alarcon, E. I.; et al. Human serum albumin as protecting agent of silver nanoparticles: Role of the protein conformation and amine groups in the nanoparticle stabilization. *J. Nanoparticle Res.* **2013**, *15*, No. 1374.
(51) McLaughlin, S.; et al. Sprayable peptide-modified silver nanoparticles as a barrier against bacterial colonization. *Nanoscale* **2016**, *8*, 19200−19203.
(52) Tao, W.; et al. Periodic silver nanodishes as sensitive and reproducible surface-enhanced Raman scattering substrates. *RSC Adv.* **2014**, *4*, 3487−3493.
(53) Siiman, O.; Bumm, L. A.; Callaghan, R.; Blatchford, C. G.; Kerker, M. Surface-Enhanced Raman-Scattering by Citrate on Colloidal Silver. *J. Phys. Chem.* **1983**, *87*, 1014−1023.
(54) Nam, K. T.; Lee, Y. J.; Krauland, E. M.; Kottmann, S. T.; Angela, M. Peptide-Mediated Reduction of Silver Ions on. *ACS Nano* **2008**, *2*, 1480−1486.
(55) Liu, J. Y.; Hurt, R. H. In release kinetics and particle persistance in aqueous nano-silver colloids. *Environ. Sci. Technol.* **2010**, *44*, 2169−2175.
(56) Khetani, A.; Momenpour, A.; Tiwari, V. S.; Anis, H. Surface Enhanced Raman Scattering (SERS) Using Nanoparticles. In *Silver Nanoparticle Applications*; Alarcon, E. I., Griffith, M., Udekwu, K. I., Ed.; Springer, 2015; pp 47−70.
(57) Kaushik, V. K. XPS core level spectra and Auger parameters for some silver compounds. *J. Electron Spectrosc. Relat. Phenom.* **1991**, *56*, 273−277.
(58) Erol, M.; et al. Communication SERS Not To Be Taken for Granted in the Presence of Oxygen SERS Not To Be Taken for Granted in the Presence of Oxygen. *Society* **2009**, 10−12.
(59) Kelly, K. L.; Coronado, E.; Zhao, L. L.; Schatz, G. C. The Optical Properties of Metal Nanoparticles: The Influence of Size, Shape, and Dielectric Environment. *J. Phys. Chem. B* **2003**, *107*, 668−667.

DOI: 10.1021/acsomega.7b00982
ACS Omega 2018, 3, 724−733